CORRELATING LASER REFLECTANCE WITH HYDRODYNAMICAL PROCESSES DURING WAVE PROPAGATION IN SHALLOW WATER USING X-RAY CT-SCANNER

Constant Pilote[1], Bernard Long[2]

Abstract

During the last four years, the aim of the project was to map sediment transport in the nearshore zone by conducting a spatial and temporal analysis of the laser reflectance on hydrodynamic coastal environments. A relationship has yet been established between sediment transport processes and airborne laser reflectance along a dune field. The aim of the present research is to correlate in laboratory the blue-green reflectance laser intensity measurement of the sea bed, the density of the sea bed and the suspended sediment concentration by measuring the density of the surface bed and the concentration of the suspended sediment by CT-scan, the suspended sediment concentration by PIV and current vector distribution during wave action on the dynamic beach profile. In this study, the use of laser reflectance and acoustic return to measure suspended sediment under waves is discussed.

Key words: Beach hydrodynamics, Laser reflectance measurement, PIV, wave propagation, X-ray CT-Scan intensity, Suspended sediment concentration

1. Introduction

Airborne LiDAR bathymetry (ALB) technology has proven to be an efficient laser-based tool for the monitoring of coastal environments and for the mapping of bathymetry, and more recently biological habitats (Collin et al. 2010, 2011) or geomorphology (Xhardé et al., 2011) and sedimentological facies (Cottin et al. 2009). It has also been used to establish a relationship between laser reflectance along a dune field and sediment transport processes (Aucoin, 2012; Aucoin et al, 2011; Long et al, 2010). In this study, we investigate the use of blue-green laser reflectance, CT-scanner density values and acoustic backscattered amplitude to measure the suspended sediment concentration (SSC) on a dynamic beach profile. For this purpose, each instrument was calibrated and used during a beach profile deformation process by waves to correlate their response with SSC. Regions of interest (ROIs) were selected and data were compared. This paper concentrates on the correlation between laser reflectance intensity (LRI) and backscattered ultrasound amplitude.

2. Material

2.1 *CT-scanner*

The CT-scanner of the facility is a Siemens' Somatom Sensation 64 mounted on rails (fig. 1). An aluminium frame can be added to the structure to support various devices and instruments.

Medical CT-scanners can be used to measure relative density of materials such as sand in geosciences and sedimentological studies (Duliu, 1999; Ketcham and Carlson, 2001; Mees et al., 2003; Duchesne et al., 2006; Montreuil and Long, 2011). The relative density is measured in Hounsfield units (HU) and varies from -1024 to 3071 (Kak and Slaney, 1999) with air and water values of -1000 and 0 HU, respectively (Ketcham and Carlson, 2001). The quartz sand used in this study has a density similar to that of human bone (1477 HU) and spinal core (1609 HU) (Schneider et al., 1996).

[1]INRS-ETE, 490 de la Couronne, Québec (Qc), Canada G1K 9A9. constant.pilote@ete.inrs.ca
[2]INRS-ETE, 490 de la Couronne, Québec (Qc), Canada G1K 9A9. blong@ete.inrs.ca

2.2 *Particle Image Velocimeter (PIV)*

The particle image velocimeter used in the experiments is a LaVision PIV. The PIV is a device constituted of a pulsed laser and two CCD cameras. The wavelength of the laser is 532 nm. It is double pulsed. The laser is focused into a thin sheet so that only the particles in the plane reflect the laser. The CCD cameras receive the reflected photons and the Davis software analyzes images.

Figure 1. CT-scanner with the flume passed in the gantry and PIV (structure is now in aluminium instead of wood)

2.3 *Acoustic Doppler Velocimeter (ADV)*

The ADV used is a Nortek Vectrino II. For this study, the data used was the Centerbeam Amplitude measure. The Vectrino II shoots a 10 MHz acoustic frequency. Usually used to know the x y and z velocities, it is used to measure the SSC in this study.

2.4 *Multibeam autonomous portable laser (MAPLE) prototype*

The MAPLE system is a prototype of LiDAR developed by the INRS in collaboration with INO (National Optical Institute) to help in the calibration of the ALB SHOALS system and relies on similar principles. An optoelectronic module emits two laser beams at 1064 nm (IR) and 532 nm (green-blue) wavelengths and a Campbell Scientific CR1000 datalogger records the backscattered energy for each wavelength as well as the respective incident laser energy, internal and external temperatures (as they affect the emitted laser energy), the range (source-target distance) and the laser beam incidence angle at a rate of 1Hz (Aucoin et al., 2011). The ratio between incident and backscattered laser energy provides information about the physical properties of the reflecting surface (Long and Robitaille, 2009).

3. Methodology

The calibration has been conducted in three different phases. First, the calibration for the Optical Backscatter Sensor (OBS), the Acoustic Doppler Velocimeter (ADV) and MAPLE is conducted in a

cylindrical tank of 120 cm of diameter and 150 cm deep. To realize this calibration, several concentrations of sand were added to clear water and put into suspension with a rotating shaft with propeller to obtain a calibration curve.

In a second experiment, the ADV was mounted in a 7 m long and 0.3 x 0.3 m inner cross section flume. The flume was filled with Ottawa sand (d_{50} = 0.147 mm) with a uniform slope of 1/15 at one end. It was passed into the gantry of a mobile medical CT-scanner and filled with 20 cm of water. Regular waves of 4 cm height and 1 s and 2 s period were made by an automated device. PIV images and ADV data were taken at four positions along the sand bed every hour for six hours.

A third experiment has been conducted under same conditions with a 1 s period wave. PIV images and scan images were taken simultaneously at five different positions every hour during six hours. MAPLE data were taken at the same places just after the images acquisition.

The ADV and the PIV images in the second experiment are used to determine the SSC by backscattered amplitude in the water column for the ADV and by LRI for the PIV. Each data collection was done over 2 s at 10 Hz for each instrument. The ADV was mounted to be at 5 cm from the sand bed. It collected 40 amplitude return data over 4 cm, every millimeter from 2 cm to 6 cm under the transmitter. The gain reduction was set to -50 dB. There was no range compensation. After each collection of data, the instruments were displaced to the other position of measurement. Data collection occurred every 15 minutes to cover each four positions into one hour. ADV data were then compared to calibration data, so SSC could be quantified. PIV took single frame images. The exposition time was 10µs. The laser power was at 100%. To obtain good images, filters of 3 x ND x 8 were used for cameras. For PIV images, a ROI corresponding to the cross section of the laser with the volume swept by the ADV signal was extracted and the LRI was averaged over every millimeter of depth to fit the same size of the ADV matrix. A Matlab program was elaborated to do this.

In the third experiment, the PIV was used as a calibration to know the SSC. The cameras were centered at the exact same place where the CT-scanner shoots its X-rays. Synchronized images of the CT-scanner and the PIV were taken. Double frames images were took at 7 Hz for 4 s, giving 28 images. Four series of 20 sequential scans of 512 x 512 x 30 voxels matrices were taken. The voxel dimension was 0.6 mm^3, giving a 30 x 30 x 1.8 cm volume scanned. Rotation time was 0.36s and cycle time 0.5s. MAPLE data were taken just after PIV and CT-scan images over a 10 s acquisition time. The MAPLE was vertical and took 250 µs of data every 1 s.

4. Results

4.1 *Calibration results*

The calibration covered concentrations ranging from 0 g/L to 50 g/L of sand. The ADV response is decreasing with depth and the curve fits a second order polynomial equation (fig. 2A). The backscattered amplitude is maximum at the first cell, that is at 2 cm from the ADV, decreases with depth and is minimum at the last cell, at 12 cm. The higher the concentration is, the faster the curve decrease in the first part of the curve. For low concentrations, the curve decrease almost linearly. For higher concentrations, the curve exhibits a fast decrease in the first two centimeters of the profile and then decreases more slowly. It's also seen, when profiles with suspended sediments are compared to the profile without sediment, that the backscattered amplitude is higher when there are suspended sediments. For a given position, when the SSC increases, the amplitude return increases and then decreases (fig. 2B). For a given concentration, the amplitude return decreases with depth.

A.

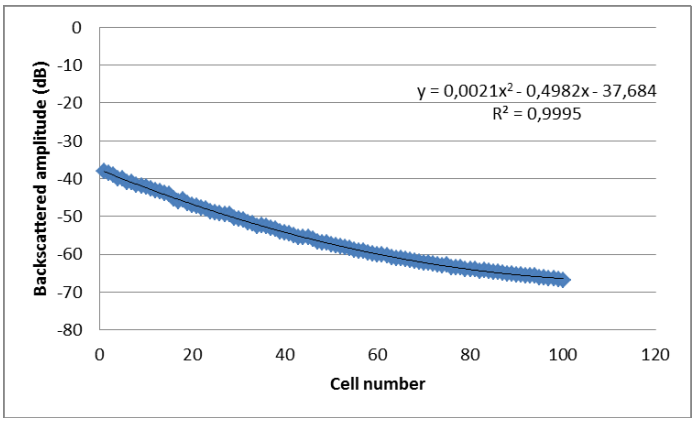

B.

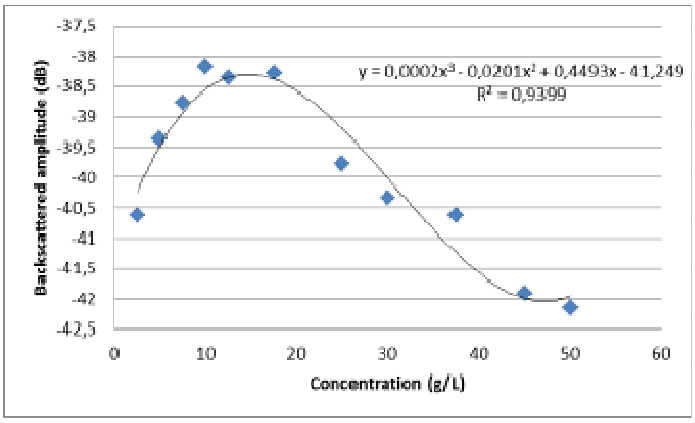

Figure 2. ADV calibration profile of attenuation A) at a given SSC (10 g/L) and B) at a given position (first cell)

For the MAPLE, the reflectance in function of the concentration followed an approximate linear equation (fig. 3). The reflectance is defined as the reflected intensity divided by the emitted intensity. When there is no sand in the tank, the reflectance is influenced by the bottom of the tank. With the mixer off, the reflectance was 0.101. With the mixer on, it dropped to 0.035. When sand is added, the reflectance increases.

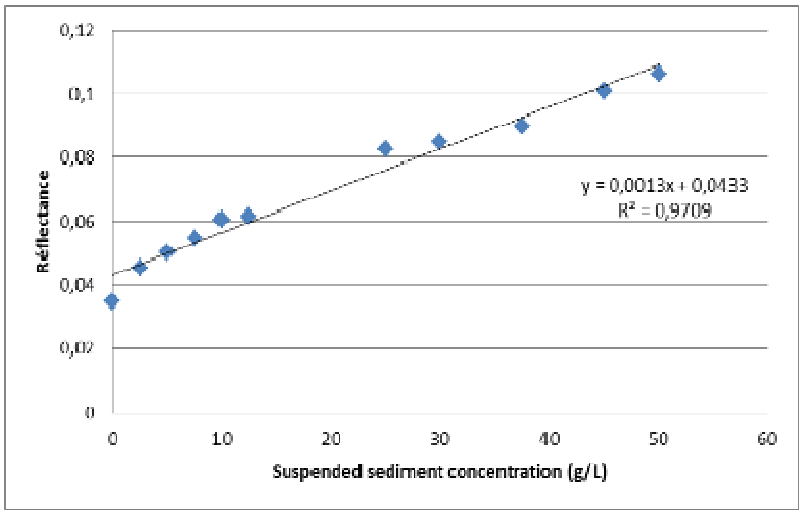

Figure 3. MAPLE calibration curve of reflectance in function of SSC

4.2 *CT-scanner and MAPLE LRI preliminary results*

Results from previous experiments tended to show that a correlation between CT-scan and LRI from MAPLE is possible. In detail, from the sequential CT images, averaged over 1 second, we defined the frontier density point (FDP) of the new image. Density profiles along the water column and along the sediment column, for waves 60 mm high and 700 ms period, show an increasing density at the frontier between SSC column and upper bedload transport zone (UBTZ) (fig. 4A). For these conditions, the LRI decreases when the density increases. The density profiles at the same station for waves 38 mm high and same period, show a difference between the water column density slope and the UBTZ density slope at the FDP (fig. 4C). At this point, LRI increases when UBTZ surface density increases. When the SSC increase the FDP value varies from 150 to 250 HU and the standard deviation (SD) is 29.05 (fig. 4B). This FDP variation is smaller if the SSC decreases and the SD is 6.12 (fig. 4D).

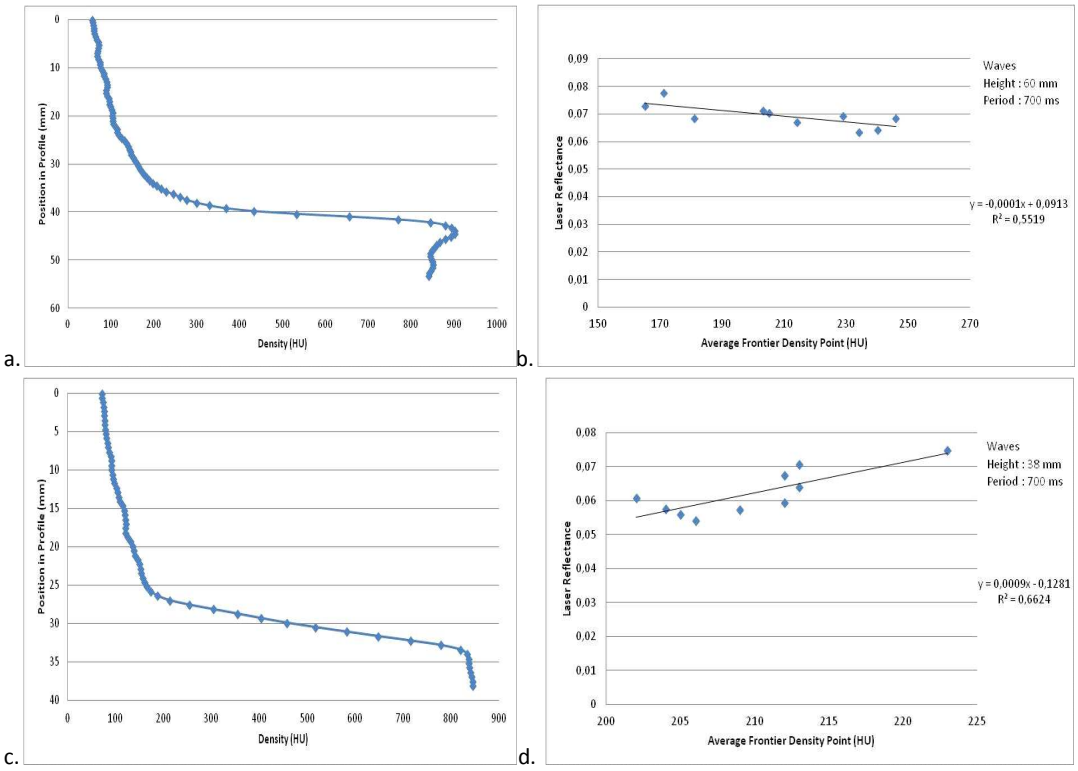

Figure 4. Profile density and laser reflectance in function of average FDP for wave height of 60 mm (*a*, *b*) and 38 mm (*c*, *d*) and period of 700 ms

4.3 *PIV images results*

PIV images display a color scale of the reflected intensity of blue-green laser (fig. 5). They were treated with a Matlab program that extracted the ROI from the images and returned a matrix of the same size as the ADV matrices. Each matrix data is the average intensity over the number of pixels contained in a 1 x 6 mm² surface, the diameter of the ADV being 6 mm and the cell depth 1 mm. The profile obtained is compared to the ADV profile (fig. 6).

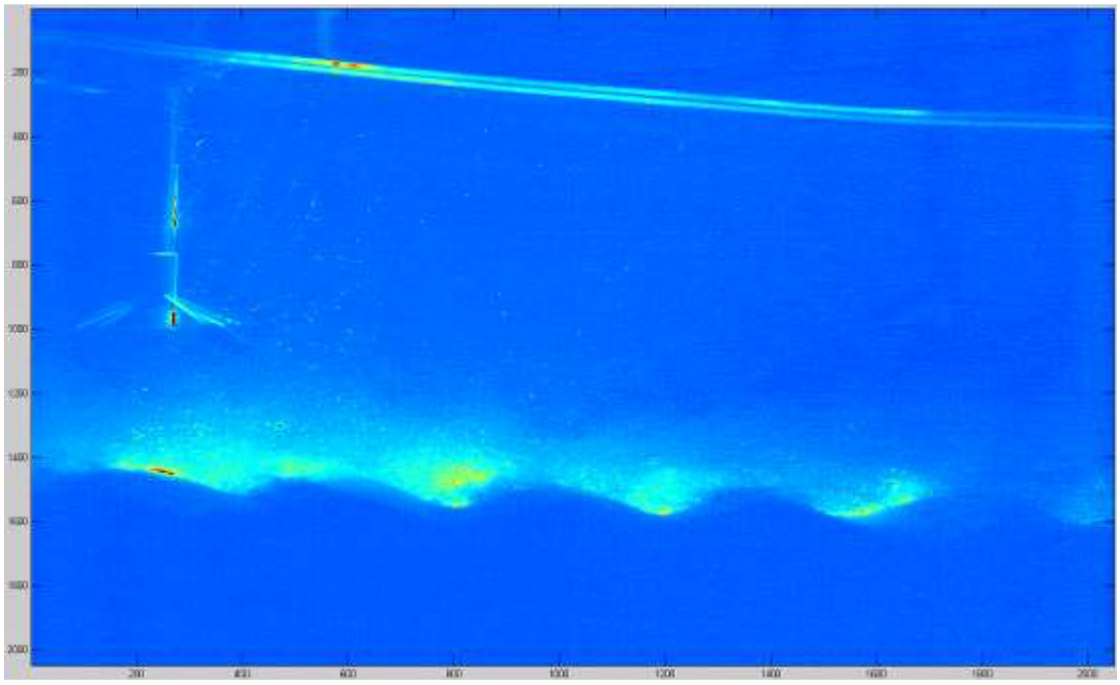

Figure 5. PIV image of the setup ripple in dark blue at the bottom, ADV left and suspended sediments reflecting the laser

The ADV profile (fig. 6B) exhibits two maxima. The first, at -58.8, in cell 12 and the second, at -18.3, in cell 30. Before and between these maxima, values are minimum. For the PIV profile (fig. 6A), there's only one maximum at the 30th cell. The profile increases from the first to the 30th cell, and then decreases until the last. The LRI value starts at 108, reaches the maximum at 160, and the minimum at 87. These data were taken in the through between two waves.

Other profiles from different moments during the passage of the wave are analyzed (fig. 6). For this case, the data were taken during a falling wave. The ADV response (fig. 6D) oscillates between -50 and -40 with a maximum in the 37th cell at -24. The PIV profile (fig. 6C) at the same time is constantly increasing from the first cell at 130 until the very high peak in the 25th cell at 353.7. It then decreases rapidly to 102.2.

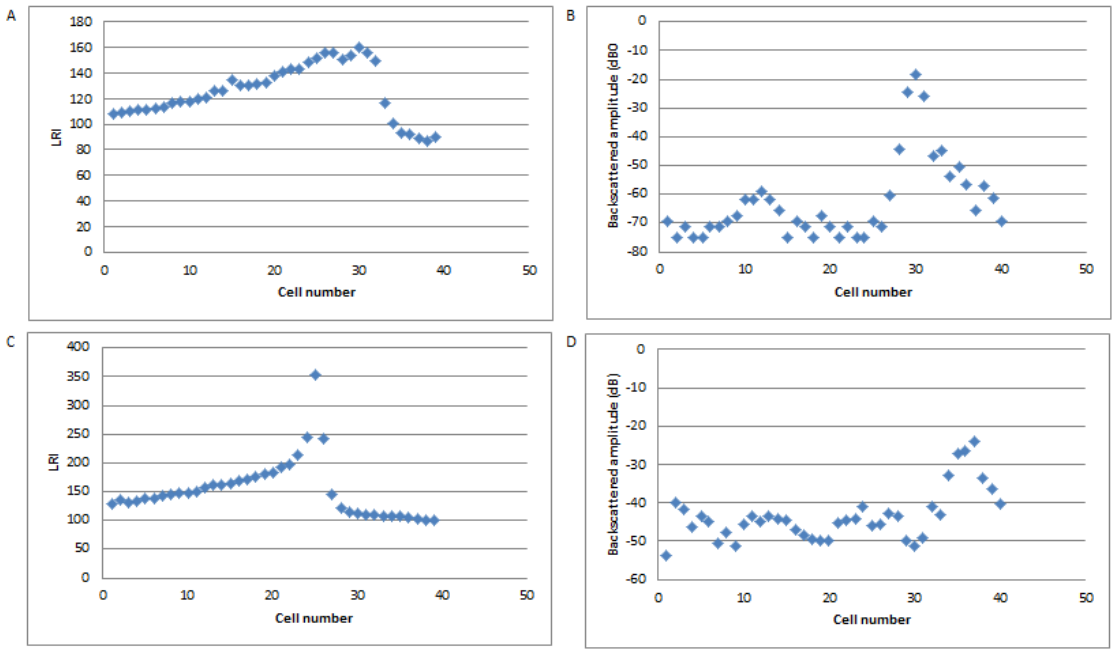

Figure 6. PIV LRI and ADV backscattered amplitude profiles in a wave through (A, B) and a falling wave (C, D)

Previous experiments with PIV gave an insight on orbital movement of water under oscillatory flow (fig. 7) with grain size (D_{50} = 0.215 mm). Figure 7 shows results of the evolution of SSC during wave propagation over a sand bed. On this experiment, PIV image showed the behavior of bedload during the passage of the wave. In the wave trough (fig. 7A), the current vectors are oriented seaward and the UBTZ is dense, and the SSC zone thickness is reduced at few millimeters. During the beginning of the climbing phase of the wave (fig. 7B), the current vectors point upward, inducing suspended sediment transport. Under the wave (fig. 7C), the current oriented landward drags a high SSC. Finally, during the falling wave phase (fig. 7D), the current penetrates toward the bed and the UBTZ density increases.

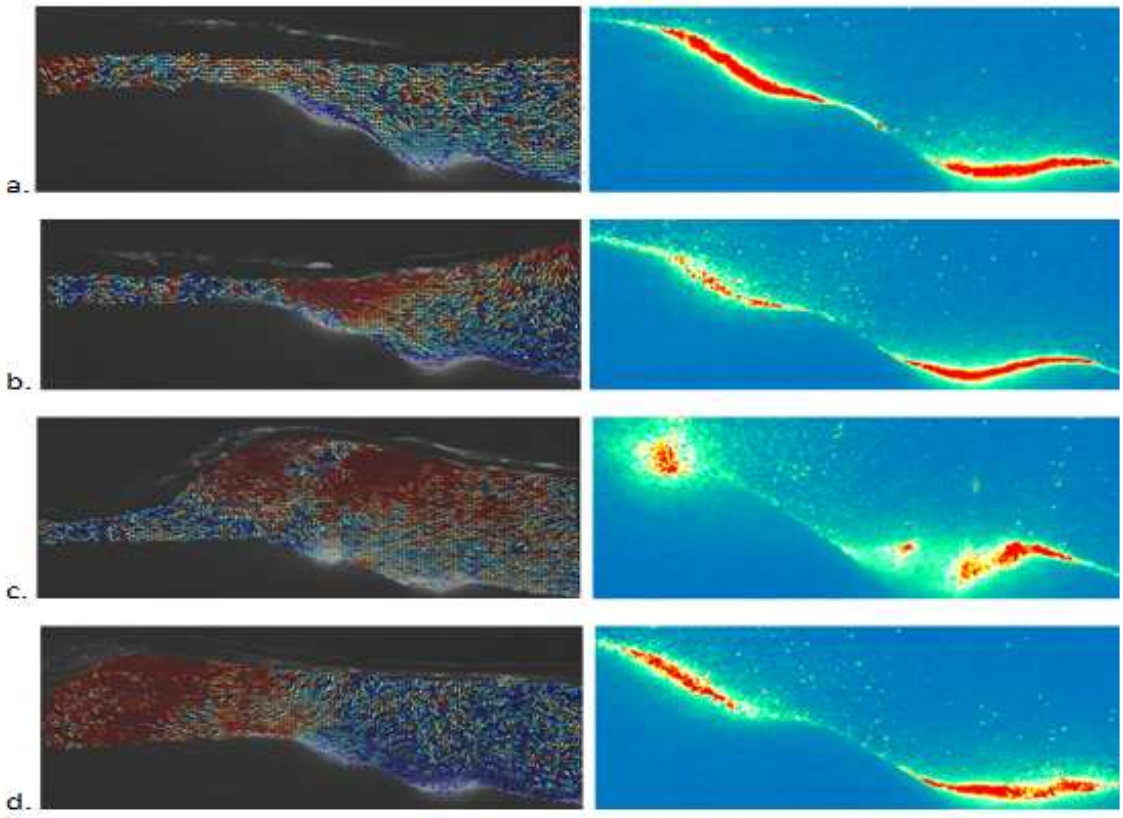

Figure 7. Vectors of current and density image of sediments obtained by PIV in *a.* wave through, *b.* rising wave, *c.* wave crest and *d.* falling wave

5. Discussion

ADV uses acoustic measurements. It is known that ultrasound is exponentially attenuated with distance with a different coefficient of attenuation depending on the medium where it travels (Martinez, 2010). The calibration profile corroborates this physical phenomenon. As the first two centimeters are not in the profile, a part of the curve is missing. The amplitude return is influenced by the SSC as more suspended sediment reflect more emitted signal for a given position. More suspended sediment also means more attenuation because the grains of a given depth prevent the propagation of the signal deeper. These two phenomenon conjugate and this is why, for a given position, backscattered amplitude rises when suspended sediment increase in low concentrations, but begins to decrease after a certain concentration. A critical concentration for a given position may exist where there is enough sediment to reflect the amplitude properly, but not too much to prevent the signal to propagate.

MAPLE calibration curve shows that LRI increases proportionally with SSC. It was already known that suspended sediment could have an influence on LRI when a shift is observed between maximum density value of a sand ripple and maximum laser beam energy (Long et al., 2010) or when higher backscattered intensities and standard deviation are observed on the crests and stoss sides of active bedforms (Aucoin et al., 2011). The calibration supports it. Still water does also reflect more light than moving water because of specular reflection. This is why the reflectance without sand is different when water is moving or not.

Montreuil et al. (2008) defined the different transport zones over a sand ripple after the study of density profiles obtained with CT-scanner images. Aucoin et al. (2011) demonstrated that laser penetrates deeper (7 mm) in pure quartz sand than in field sand (98% absorbed in the first millimeter). LRI can be affected by various factors such as SSC, grain mineralogy, granulometry and grain compaction. High waves drag more

sediment and induce more erosion of the beach, thus putting more sediment in suspension. In figure 4A the density profile along the water column densifies smoothly. The FDP range is large, and thus the FDP standard deviation, because the varying SSC influences the FDP value. A small FDP means less SSC and a high FDP more SSC. For these conditions, the LRI is slightly decreasing when the FDP increases, suggesting that the sand bed have a higher incidence on reflected light than the suspended sediments. Hence, when the FDP is low, the SSC is low, and the LRI is reflected on the bed, so it is higher. When the FDP is high, the SSC is high and the LRI is more attenuated and less light reaches the bed, so its value decreases. In the same logical, with smaller waves, the beach will be less eroded and there will be less sediment in suspension. The density profile in figure 4C shows a more drastic change of slope at the FDP. This is because there is less sediment in suspension, so the density in the water column practically doesn't change until the bottom is reached. The FDP range is also more concentrated and the standard deviation is small, because it's not influenced by SSC, but only by the bottom density. In these conditions, the LRI is not attenuated because there is not enough suspended sediment. It is the bottom density that influences the LRI. Aucoin et al. (2011) demonstrated that the compaction and density of the bedform influences the LRI. So LRI increases when bed density increases. During high waves climate, the erosion of the UBTZ is more important than during a small wave climate, and the SSC increases. By consequence the LRI decreases.

For the PIV and ADV results, the highest peaks occur when the signal touches the bed. After this peak, the signal is almost zero because it is in the sand. Both ADV and PIV can determine where the bottom is. A cloud of suspended sediment is visible on the ADV profile, but not on the PIV profile. Data and profiles show that the ADV can record the variations of SSC in the water column, where the PIV can't. The PIV seams to integrate over the distance. It doesn't discriminate the SSC in the profile. The method should be revised, as it can be a problem of the averaging, where we lose the punctual information of suspended sediment LRI in the rest of non-lighted pixels data.

PIV vector images show the orbital movement of an oscillatory flow. During a wave passage, an orbital water movement is observed. This orbital movement is similar to the vortex observed in the front of a ripple during a steady flow experiment conducted below CT-Scan and PIV (Long and Montreuil, 2011). The authors show that vortices activity can be subdivided in three phases: the intrusion phase, the water migration phase and the expulsion phase. During the intrusion phase, the sediment poor fluid (lowest concentration) is dragged downward and begins to apply pressure that deepens the critical shear stress (Long and Montreuil, 2011). During the water migration phase the pore pressure vector is parallel to ripple surface and represents the longitudinal part of the vortex. During the expulsion, water is ejected from the sediment during the vortex evolution. From this, during the liquefaction phase, the porosity inside the sediment increases and goes deeper. This phenomenon causes the erosion of the superficial sediment and an active suspended sediment transport. Figure 7 demonstrates this. The use of PIV to know vector distribution and qualitative suspended sediment distribution is confirmed.

6. Conclusion

This study brought information on the feasibility to measure SSC under an oscillatory flow on a dynamic beach profile with different instruments and techniques. The calibration showed that both acoustic backscattered amplitude from ADV and LRI from MAPLE respond to SSC. Experiments showed that suspended sediments are visible on CT-scanner density profiles as these profiles were different for different wave heights. MAPLE results showed that LRI can be affected more or less by the suspended sediments and the bedload. ADV backscattered amplitude can be used to measure the variations of suspended sediment in the water column, but correlating the results with the SSC value is difficult due to the decreasing curve with depth and the changing response with concentration of backscattered amplitude. PIV is useful to map vectors of displacement of suspended sediment, but the technique used failed to map the variations of suspended sediment in the water column.

Experiments should be done to know exactly the penetration depth of MAPLE for different concentrations. It would then be easier to expect if the laser is either reflected by suspended sediment or bottom. More research should also be done on the backscattered amplitude of ADV due its capacity to map the SSC variations. Finally, a more reliable analysis of PIV images should be done to obtain SSC variations.

Acknowledgements

This project was funded by the Canadian Innovation fund. The authors wish to thank Louis-Frédéric Daigle, Mathieu Des Roches and Seiya Suenaga for their contribution in experiments setup, data acquisition and analysis. A special thanks to Professor Yves Gratton for his scientific support.

References

Aucoin, F., Long, B., Xhardé, R. and Collin, A., 2011. Using airborne LiDAR bathymetry to map coastal hydrodynamics processes, *Coastal Sediments* (3), 2479-2491

Aucoin, F., 2012. Utilisation du LiDAR bathymétrique pour la determination des processus hydrodynamiques, *INRS-ETE*, M.Sc. thesis, Québec, 124 p.

Collin, A., Long, B. and Archambault, P., 2010. Salt-marsh characterization, zonation assessment and mapping through a dual-wavelength LiDAR. *Remote Sensing Environment*, 114:520-530

Collin A, Archambault P. and Long, B., 2011. Predicting species diversity of benthic communities within turbid nearshore using full-waveform bathymetric LiDAR and machine learners, *PLos ONE*, 6 (6): e21265

Cottin A.G., Forbes D.L., and Long B.F., 2009. Shallow Seabed Mapping and Classification using waveform analysis and bathymetry from SHOALS LiDAR data. *Canadian Journal of Remote Sensing*, 35 (2): 422-434

Duchesne, M.J., Long, B.F., Labrie, J. and Simpkin, P.G., 2006. On the use of computerized tomography scan analysis to determine the genesis of very high resolution seismic reflection facies, *Journal of Geophysical Research* 111, B10103, doi: 10.1029/2006JB004279

Duliu, O.G., 1999. Computer axial tomography in geosciences: an overview, *Earth-Science Reviews* 48, 265-281

Kak A. C. and Slaney, M., 1999. Principles of computerized tomographic imaging, *IEEE PRESS*, New York, 329 pp.

Ketcham, R.A. and Carlson, W.D., 2001. Acquisition, optimization and interpretation of X-ray computed tomographic imagery: applications to the geosciences, *Computers & Geosciences* 27, 381-400

Long, B.F. and Robitaille, V., 2009. Use of a multi-beam autonomous portable laser equipment (MAPLE) to measure the reflectance of shallow water facies and habitats – a new tool to calibrate airborne laser bathymetry instruments, *Proceeding of the 2nd FUDOTERAM Workshop* (Québec, Canada)

Long, B.F., Aucoin, F., Montreuil, S. and Xhardé, R., 2010. Airborne LiDAR bathymetry applied to coastal hydrodynamic processes, *Proceedings of ICCE 2010*, Shanghai, China

Long, B. and Montreuil, S., 2011. Vortex activity influences the pseudo liquefaction of the lower stoss-side ripple surface. Measurement by CT-scan, *ICMG proceeding*

Martinez, R., Leija, L., Vera, A., 2010. Ultrasonic attenuation in pure water : comparison between through transmission and pulse-echo techniques, *Health Care Exchange (PAHCE), 2010 Pan American*, p. 81-84

Mees, F., Swennen, R., Van Geet, M. and Jacobs, P., 2003. Applications of X-ray computed tomography in the geosciences, *Geological Society of London Special Publication* 215

Montreuil, S., Long, B. and Kamphuis, J.W., 2008. Surface density variations along a sand ripple under stationary flow measured by CT-scanning, *Coastal Engineering* (3), 2659-2671

Montreuil, S. and Long, B., 2011. Relationship between vortex activity and pseudo liquefaction at a lower stoss-side ripple surface, *Coastal Sediments* (2), 1121-1134

Schneider, U., Pedroni, E. and Lomax, A., 1996. The calibration of CT Hounsfield units for radiotherapy treatment planning, *Physics in Medicine and Biology* 41, 111-124

Xhardé, R., Long, B.F., and Forbes, D.L., 2011. Short-term beach and shoreface evolution on a cuspate foreland observed with airborne topographic and bathymetric LiDAR, *Journal of Coastal Research*, SI 62, p.50-61